

The evolution of deformation twinning microstructures in random face-centered cubic solid solutions

Ritesh Jagatramka

Junaid Ahmed

Matthew Daly*

*Department of Civil, Materials, and Environmental Engineering, University of Illinois Chicago –
842 W. Taylor St., 2095 ERF (MC 246), Chicago, IL, 60607, United States*

ABSTRACT

The varied atomic arrangements in face-centered cubic (FCC) solid solutions introduce atomic-scale fluctuations to their energy landscapes that influence the operation of dislocation-mediated deformation mechanisms. These effects are particularly pronounced in concentrated systems, which are of considerable interest to the community. Here, we examine the effect of local fluctuations in planar fault energies on the evolution of deformation twinning microstructures in randomly arranged FCC solid solutions. Our approach leverages the kinetic Monte Carlo (kMC) method to provide kinetically weighted predictions for competition between two processes: deformation twin nucleation and deformation twin thickening. The kinetic barriers underpinning each process are drawn from the statistics of planar fault energies, which are locally sampled using molecular statics methods. kMC results show an increase in the fault number densities of solid solutions relative to a homogenized reference, which is found to be driven by the fluctuations in planar fault energies. Based on kMC relations, an effective barrier model is derived to predict the competition between deformation twinning nucleation and thickening processes under a fluctuating planar fault energy landscape. A key result from this model is a measurement of the length-scale over which the influence of local fluctuations in planar fault energies diminish and nucleation/thickening-dominated behaviors converge to bulk predictions. More broadly, the tools developed in this study enable examination of the influence of chemistry and length-scale on the

*Corresponding author: mattdaly@uic.edu (M. Daly)

evolution of deformation twinning mechanisms in FCC solid solutions.

Keywords: Deformation Twinning; Concentrated Solid Solutions; Molecular Dynamics; Molecular Statics; Kinetic Monte Carlo Simulations; Stacking Fault Energy.

1. INTRODUCTION

The activation of deformation mechanisms in metallic materials is determined by a complex interplay between applied stresses, microstructure effects, and energetic process barriers that resist mechanism operation. The latter element can be conceptualized using the generalized planar fault energy (GPFE) landscape,^{1,2} which relates the critical planar fault energies (i.e., stacking fault and twinning fault energies) to the sequenced shearing of crystallographic planes. Subsequent investigations have leveraged this planar fault energy concept to provide analytical descriptors for the activation of dislocation-mediated mechanisms, which are relevant in face-centered cubic (FCC) materials. Notable examples include investigations from Rice³ and Ogata et al.⁴, where the critical fault energies of the GPFE landscape are used to predict the stresses for dislocation nucleation from a crack tip and a twin boundary, respectively. Building on the crack tip model of Rice,³ Tadmor and Hai⁵ showed that the competition between trailing partial and twinning partial dislocation emission is controlled by the ratio of unstable stacking and twinning fault energies. This effort produced a first principles-based metric to evaluate the incipient competition between deformation twinning and dislocation slip. This ‘twinability’ criterion has been homogenized over a distribution of crack-tip orientations and crystal textures.⁶ Later works have applied similar GPFE-based criteria to consider the competition between grain boundary-mediated mechanisms in nanocrystalline materials⁷ and the evolution of mechanism competition beyond incipient plasticity events.⁸ Building on this concept, Daly et al.⁹ demonstrated how the competition between nucleation and thickening of deformation twins in FCC metals may also be determined by the

magnitudes of the critical planar fault energies of the GPFE landscape.

While these contributions have provided important fundamental insights into mechanism competition, one limitation in these works is the restriction in applicability to the study of unary metals, where deformation twinning has limited engineering applications. Yet, with the ubiquity of complex alloys, an expansion of deformation twinning theory to predict deformation tendencies in these systems is of significant technological relevance. For instance, profuse twinning is known to underpin the exceptional work hardening of the twinning-induced plasticity (TWIP) steels.^{10,11} Important studies on the TWIP effect include works from Bouaziz and co-workers,^{12–18} and Steinmetz et al.,¹⁹ with the status of these materials summarized in reviews from De Cooman and co-workers.^{20,21} Twinning is also cited as a contributing mechanism in the plasticity of several medium and high entropy alloy (MEA and HEA) systems (e.g., CoCrFeMnNi,^{22–27} CoCrNi,^{27–30} and FeMnCoCr^{31–33}). While previous works provide some guidance for the deformation twinning tendencies of these materials – that is, these materials profusely twin due to low stacking fault energies (e.g., as in Refs.^{10,11,22,34,35}) – this interpretation is not entirely consistent with a careful examination of the literature. For instance, the stacking fault energies of TWIP steels and deformation-twinned HEAs generally fall in the range of $\sim 20\text{--}60\text{ mJ/m}^2$ ^{20,21} and $18\text{--}45\text{ mJ/m}^2$,^{36,37} respectively. This range overlaps with the reported values for pure Cu ($\sim 36\text{ mJ/m}^2$).³⁸ Yet, except under dynamic loadings or when nanostructured, Cu is not observed to exhibit significant deformation twinning.³⁹

The recent literature offers a partial explanation for this discrepancy between twinning behaviors in pure and multicomponent low stacking fault energy materials. For instance, dramatically different values for the stacking fault energy of equimolar CoCrNi have been observed, with large negative values of -62 mJ/m^2 up to 22 mJ/m^2 being reported.^{30,40–42} These

large variations have been linked to the varied arrangement of atoms in solid solutions, which gives rise to a distribution of planar fault energies that vary locally within fault planes.^{43–47} Zhao et al.⁴⁶ have used density functional theory (DFT) to analyze the effect of random atomic arrangements on the ‘local’ intrinsic stacking fault (ISF) energy and reported fluctuations up to 200 mJ/m² for NiFe, NiCo, and CoCrNi systems. This finding is supported by our recent work, which has examined the statistical relationships between solute arrangement and fluctuations in fault energies.⁴⁸ Collectively, these reports highlight the large scatter that can arise in planar fault energies due to solute arrangement, which is a behavior unique to multicomponent systems. Within the context of dislocation-mediated deformation mechanisms, local deviations in planar fault energies are significant as they provide new kinetic pathways for mechanism evolution.⁴⁹ The implications of local fluctuations on the fault energies of solid solutions raise an interesting question: how do these local fluctuations drive the behavior of deformation mechanisms mediated by the GPFE landscape?

Here, we examine this question through a study of the evolution of deformation twinning microstructures in randomly-arranged concentrated solid solutions. To capture this evolution, we implement kinetic Monte Carlo (kMC) simulations to measure the competition between nucleation and thickening of deformation twins. A key feature of this approach is that it enables a local definition and evaluation of the process barriers of deformation twinning, which we align to match the statistical distribution of critical planar fault energies that are obtained directly from GPFE landscape. Furthermore, we define a set of effective planar fault energies using analytical methods, which account for the variations in deformation twinning microstructures that arise from local fluctuations. This methodology is independently validated by tensile testing of nanowires using molecular dynamic (MD) simulations. The results of this work provide insights into the evolution

of deformation twinning microstructures within a spatially heterogeneous process barrier landscape.

2. METHODOLOGY

We have selected the NiCo system to investigate the influence of a heterogeneous process barrier landscape on the evolution of deformation twinning microstructures. This choice was made because the NiCo system possesses solid solubility over wide ranges of concentrations and is well documented to exhibit deformation twinning.^{50,51} Furthermore, interatomic potentials are readily available to model planar faults for this system, which facilitates the atomistic simulations described in the subsequent sections. Our study is performed using an equimolar composition of NiCo binary alloy to maximize solute dispersion. Yet, the approach outlined herein can be expanded to different single-phase solid solutions with arbitrary compositions and numbers of components (e.g., MEAs and HEAs), for which accurate potentials exist to model bonding interactions.

2.1 Molecular static simulations

The fluctuations in the GPFE landscape are quantified using molecular statics (MS) simulations, which are implemented using the Large-scale Atomic/Molecular Massively Parallel Simulator (LAMMPS).⁵² The Open Visualization Tool (OVITO)⁵³ was used to visualize the atomic topologies and common neighbor analysis was performed in OVITO to identify the faulted structures. Atomic interactions in the NiCo system are modeled using the embedded-atom method (EAM) with an interatomic potential developed by Béland et al.⁵⁴ This potential has been validated by comparing the system-level GPFE landscape to first-principles density functional theory calculations (see Section S1, Figure S1 in the Supplementary Materials). Equimolar NiCo systems measuring 12 by 12 by 5 nm in the x , y , and z directions, respectively, were constructed to measure

the GPFE landscape. Figure 1 provides a schematic of the system used in MS simulations. We have validated the overall system sizes through sensitivity analysis (see Section S2, Figure S2 in the Supplementary Material). The equimolar systems are modeled such that the $\langle 1\bar{1}0 \rangle$, $\langle 11\bar{2} \rangle$, and $\langle 111 \rangle$ crystallographic directions are aligned to the global x , y , and z axes, respectively. The GPFE landscape is obtained through a three-stage rigid shearing process, where the total rigid shear per stage is equal to the Burger's vector of a $\langle 112 \rangle$ -type Shockley partial dislocation (*i.e.*, $\frac{a_o}{\sqrt{6}}$, where $a_o = 0.351$ nm is the lattice parameter). Each stage is executed over 100 shearing increments to capture the intermediate configurations of the GPFE landscape. In between each shearing step, the system is relaxed in the z -direction and the per atom potential energies are recorded. Initially, an ISF is formed by displacing two halves of the NiCo crystal along the $\langle 11\bar{2} \rangle$ direction within the $\{111\}$ shear plane. Adjacent layers of the crystal are sequentially sheared to form an extrinsic stacking fault (ESF) and a twin fault (TF). Periodic boundary conditions are enforced on the x and y boundaries and the z surfaces are free surfaces. The GPFE landscape is calculated from the excess energy, using the following relation:

$$\gamma = \frac{U - U_0}{A} \quad (1)$$

where U is the energy of faulted state, U_0 is the energy of the initial, defect-free system, A is the area of the fault plane, and γ is the area normalized fault energy at a given shearing step. All MS simulations are performed at 0 K. This procedure for GPFE landscape determination is well-established in the literature.^{55,56}

The local planar fault energy arises from the variations in atomic arrangements in the vicinity of the planar fault. To capture this effect, we define the local planar fault energy (γ^*) using a relation analogous to Eq. (1) and measure γ^* by sampling the GPFE landscape over a local area of

A^* in the $\{111\}$ plane (see Figure 1). For the results presented in the main text, A^* is taken as $(\sqrt[3]{10} b_{112})^2$, where b_{112} is the magnitude of the $\langle 11\bar{2} \rangle$ Burger's vector for a Shockley partial dislocation. This selection is derived from an estimate for the activation area of a partial dislocation, which we obtain from the cubic activation volume of $\sim 10b_{112}^3$. Activation volumes in the range of $1-15b_{112}^3$ have been reported in the literature for similar dislocation processes.^{57,58} As shown in this study and our previous work,⁹ an activation volume of $10b_{112}^3$ delivers self-consistent predictions for dislocation-mediated deformation twin nucleation and thickening processes. Local sampling of faulted systems resulted in ≈ 15500 samples per shear increment. As anticipated, GPFE measurements converge and fluctuations vanish, as A^* approaches A (see Section S3, Figure S3 in the Supplementary Material). It should be noted that the z -axis dimension is selected conservatively and does not influence local measurements, when above a minimum threshold. That is, the GPFE landscape emerges from differences in atomic site energies that arise due to a change in local topology during shearing. These shearing-induced excess energy contributions decay significantly within five nearest neighbors of the planar fault (about 2-3 $\{111\}$ planes),⁴⁸ which is similar to the linear dimension of the activation volume ($\sqrt[3]{10} b_{112}$, about 2 $\{111\}$ planes). Consequently, selection of a sampling dimension larger than this threshold along $\langle 111 \rangle$ introduces negligible changes in excess energy to Eq. (1).

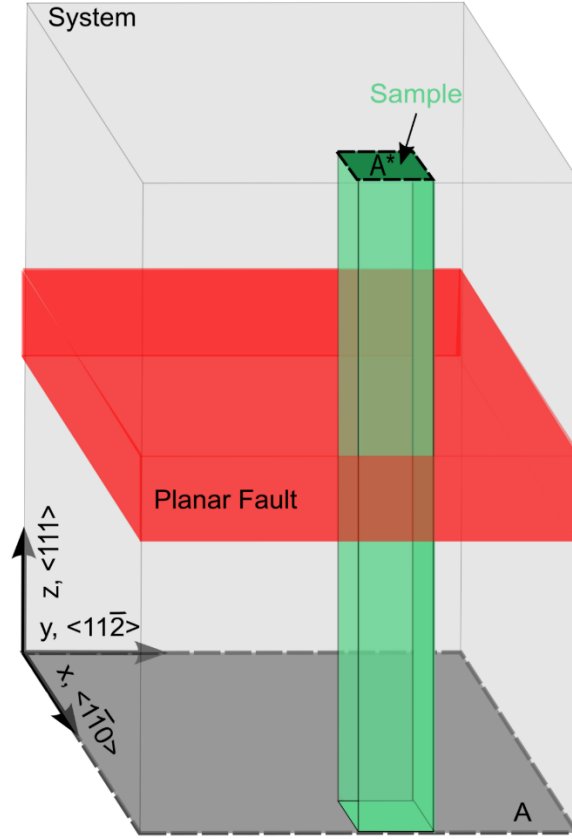


Figure 1: Schematic showing the system and sampling strategy used in MS simulations to measure the local GPFE landscape in the NiCo samples. The relevant crystal directions and fault structures are shown. The system area (A) and sample area (A^*) are shaded in grey and green, respectively and bounded by dashed stroke.

2.2 Kinetic Monte Carlo Model

To predict the effect of local variations in atomic arrangement on the evolution of deformation twinning microstructures, we have expanded a kMC model developed previously by our group for unary systems. Using the algorithm proposed by Bortz et al.,⁵⁹ this model predicts the evolution of deformation twinning microstructures by kinetically weighted selection of deformation twin nucleation or thickening processes. This kinetic weighting is determined from the process barriers for each activation event, which is defined by their dislocation mechanics, as described below. Each of these dislocation-mediated processes is considered in a discretized two-dimensional simulation cell that is defined along the relevant crystallographic directions for deformation twinning-based plasticity in FCC materials. An important aspect of our approach is that it focuses

on the intrinsic competition between deformation twin nucleation and thickening along a single twin system, while removing convoluting extrinsic factors such as microstructure heterogeneities (e.g., stress concentrations at crack tips and grain boundaries) and Schmid effects. Furthermore, competing mechanisms such as trailing partial dislocation emission, dislocation cross-slip and dislocation constrictions/reactions are not considered, as they would complicate a direct comparison of nucleation and thickening phenomena. Given this framework, this approach is most accurate for FCC single crystals where deformation twinning is prevalent along a single twin system. A complete description of the basic method, assumptions, and its limitations are provided in Refs.^{8,9} A summary of the model updates and specific assumptions to accommodate fluctuating process barriers are outlined below.

kMC simulations were performed on a NiCo single crystal with axes aligned to the $\langle 11\bar{2} \rangle$ and $\langle 111 \rangle$ crystal directions, respectively. This arrangement allows the study of mechanistic competition along the $\langle 1\bar{1}0 \rangle$ zone axis and mirrors the configuration of MS simulations. In the kMC model, the crystal is discretized such that the nucleation and movement of defects require a local process barrier to be overcome. These characteristics are well-suited to the objectives of this work as they enable a variable process barrier to be mapped to the kMC mesh. The kMC simulation cell dimensions measure Mb_{112} and Nd_{111} , where d_{111} is the interplanar spacing of $\{111\}$ planes, and M and N are integers. The simulation cell is designed with free surfaces along the y -axis and periodic boundaries along the z -axis. A schematic of the kMC simulation cell is provided in Figure 2a. The kMC mesh is discretized into regions measuring $\sim (\sqrt[3]{10} b_{112})^2 \text{ nm}^2$, which follows from the sampling area selected in MS simulations.

In kMC simulations, deformation twinning is realized through the activation of two dislocation processes: partial dislocation nucleation and glide. All the dislocations considered in this study are

90° leading <112>-type Shockley partials. Deformation proceeds through the nucleation and glide of leading dislocations from the free surface at the $y = 0$ boundary. The incipient nucleation and glide of a leading partial dislocation forms an ISF. Subsequent nucleation and glide events along adjacent {111} planes lead to the formation of a two-layered ESF and a multi-layered TF. The process barriers required to nucleate these faults are discussed in the subsequent paragraphs. Surface-based deformation twinning applies to a diverse set of systems including nanowires,^{60–64} TWIP steels,⁶⁵ nanostructured FCC^{66–68} and body-centered cubic,⁶⁹ and hexagonal close-packed metals.⁷⁰ This twin nucleation route bears some resemblance to the defect nucleation models proposed by Weinberger and co-workers^{71,72} and Sehitoglu and co-workers^{25,26} with some differences in the treatment of the process barrier. Dislocation nucleation and glide processes are considered along a single twin system to study the intrinsic competition between deformation twin nucleation and thickening mechanisms while suppressing extrinsic microstructure and loading (i.e., Schmid) factors, as previously discussed. These simplifications are intentional as they enable the effect of variable process barriers on deformation twinning processes to be isolated and directly studied. However, it should be noted that our method is sufficiently general to include extrinsic factors (e.g., far-field loading effects or Schmid factors) with some effort.

Following the method of Ogata et al.⁴, the process barriers used in the kMC model are taken from the differences of critical planar fault energies in the GPFE landscape (see Figure 2b). As shown in the figure, the first process barrier in deformation twinning ($E_1 = \gamma_{usf}^1$, where γ_{usf}^1 is the unstable stacking fault energy) is overcome to nucleate a single layer ISF. Thickening of the ISF proceeds by overcoming additional process barriers ($E_2, E_3, \dots, E_\infty$) that are defined by the difference between the relevant stable fault energy and the peak unstable energies of the subsequent defect along the GPFE landscape. The unstable fault energies that must be overcome to form one-

and two-layer faults are denoted as γ_{usf}^1 and γ_{usf}^2 , respectively. γ_{utf}^3 and γ_{utf}^∞ refer to the unstable twinning fault energies required for the formation and thickening of a deformation twin. γ_{isf} , γ_{esf} , and γ_{tf} are defined as the stable fault energies of the related faults (*i.e.*, ISF, ESF, and TF). γ_{utf}^∞ and γ_{tf} represent the energies related to a single boundary in a thickened deformation twin comprised of two non-interacting twin boundaries, with the former energy approximated as $\gamma_{utf}^\infty \approx \gamma_{utf}^3 - \gamma_{tf}$. In FCC materials, the GPFE landscape is known to stabilize after the formation of an ESF.⁴ Therefore, the process barrier for E_∞ is taken to define the thickening of deformation twins beyond three layers such that $E_\infty \approx \gamma_{utf}^3 - 2\gamma_{tf}$. Thus, the relative competition between nucleation and thickening of deformation twins is defined here by the process barriers E_1 (nucleation) and E_2 , E_3 , and E_∞ (thickening), respectively.

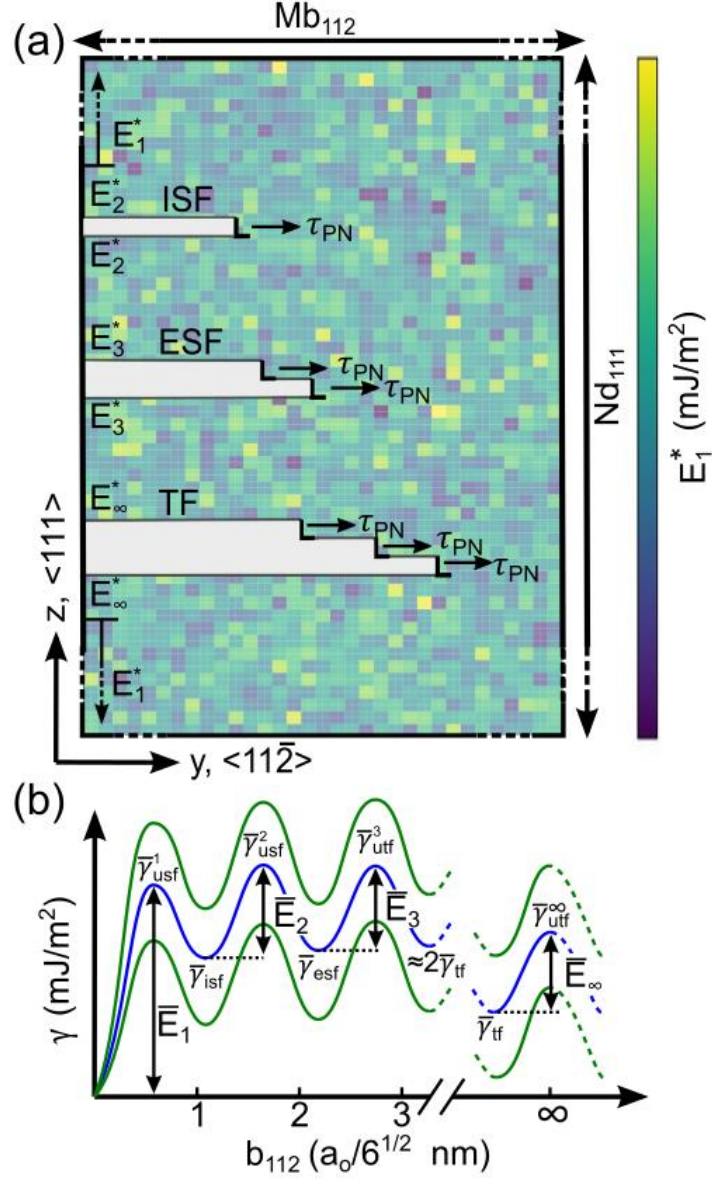


Figure 2: (a) The kMC simulation cell with the relevant crystal directions and geometric parameters noted. The color patches depict the discretized local value of the process barrier, with E_1^* shown here as an example. A schematic of the fault structures of deformation twinning (*i.e.*, ISF, ESF, and TF) are shown, along with the associated process barriers for nucleation and thickening of deformation twins, and dislocation glide stresses. The determination of process barriers is defined by the deformation history and local critical energy values at position i,j in the discretized kMC simulation cell. (b) A schematic of a variable GPFE landscape for an FCC solid solution. The blue lines represent the system average, and the green lines indicate statistical scatter (1 standard deviation). The average critical energies and process barriers are indicated with an overline. The definitions of the process barriers from the differences of critical planar fault energies are also shown.

To simulate the mechanistic competition using kMC simulations, the kinetics of nucleation and glide events are required. The rates of nucleation and glide ($R(i,j)$) operating at the i^{th} activation site in the j^{th} slip plane of the simulation cell are determined using an Arrhenius relationship:

$$R(i, j) = R_0 \exp \left\{ \frac{-[\hat{\tau}(i, j) - \tau(i, j)]V}{k_b T} \right\} \quad (2)$$

where R_0 is the Debye frequency,⁷³ k_b is the Boltzmann constant, T is the temperature (set at 300 K), $\hat{\tau}(i, j)$ and $\tau(i, j)$ are the process barrier and elastic shear stresses, respectively, and V is the activation volume (taken as $10b_{112}^3$). Under this framework, if a Shockley partial dislocation is not present in the j^{th} slip plane, then $\hat{\tau}(i, j) = \hat{\tau}(0, j)$, which represents the process barrier stress for the nucleation or thickening of a deformation twin. This shear stress can be calculated from the process barriers of the GPFE landscape using the athermal nucleation relations of classic dislocation theory.⁷⁴ Conversely, if a Shockley partial dislocation is present in the j^{th} slip plane then $\hat{\tau}(i, j)$ represents the barrier to glide for a dislocation centered at the i^{th} activation site, as given by the Peierls-Nabarro stress (τ_{PN} , see Figure 2a).⁷⁵ Thus, the conditional definition of process barrier $\hat{\tau}(i, j)$ is as follows:

$$\hat{\tau}(i, j) = \begin{cases} \frac{\pi E_k(i, j)}{b_{112}}, & \text{nucleation/thickening} \\ K_\rho \frac{b_{112}}{\rho} \exp \left\{ \frac{-2\pi \varsigma_\rho(i, j)}{\rho} \right\}, & \text{glide} \end{cases} \quad (3)$$

where, $E_k(i, j)$ is the process barriers required to nucleate or thicken a fault at i^{th} activation site in the j^{th} slip plane as described in the previous paragraph, and k is the index of the relevant process barrier as defined by the deformation history of the kMC system. The additional terms in the glide relation are defined as follows: ρ represents the distance between adjacent atomic rows along the shear direction (*i.e.*, $\rho = \frac{3}{2}b_{112}$), K_ρ is an elastic constant given by $K_\rho = \frac{G}{(1-\nu)}$, where, G and ν are the shear modulus and Poisson's ratio respectively, and $\varsigma_\rho(i, j) = \frac{K_\rho b_{112}^2}{4\pi^2 E_k(i, j)}$ represents the half-width of the dislocation core. All constants related to dislocations are defined using an edge character. The elastic constants are determined from the relevant components of the cubic

stiffness tensor available in Li and Wang⁷⁶, which are then homogenized to provide the effective isotropic shear modulus and Poisson's ratio using the method of Bacon and co-workers.^{77,78} Following the Volterra approach,⁷⁴ the internal shear stress $\tau(i, j)$ is calculated from the additive elastic field stress contributions of active dislocations in the kMC simulation cell. Free surface effects are considered by modifying the Volterra solutions to include image dislocations that enforce vanishing shear stress along the $\langle 11\bar{2} \rangle$ boundaries in the simulation cell, as in previous work.⁹ The relevant material parameters for the kMC models are given in Table I.

Table I: NiCo material parameters used in kMC simulations.

a_o (nm)	b_{112} (nm)	d_{111} (nm)	G (GPa) ^a	ν ^a	R_o ($10^{13}/s$) ^b
0.351	0.143	0.203	92.4	0.344	9.88

^aCalculated based on stiffness constants from Ref.⁷⁶ using the method of Bacon and co-workers.^{77,78}

^bTaken from pure nickel from Ref.⁹

To evaluate the influence of process barrier fluctuations on the evolution of deformation twinning microstructures, two different types of kMC simulations are performed, which are referred to here as the homogeneous and heterogeneous models. In the homogeneous model, the deformation kinetics are calculated using the average values for the process barriers. For instance, the barrier to nucleate an ISF becomes $E_k = \bar{E}_1 = \bar{\gamma}_{usf}^1$, where $\bar{\gamma}_{usf}^1$ is the average unstable stacking fault energy obtained using the methods described in Section 2.1. The other process barriers required for fault thickening are similarly taken from their average values, $E_k = \bar{E}_k$. Under the heterogeneous definition, a distribution of local process barriers is created using the statistics measured during MS sampling of the GPFE landscape. For example, the process barrier for the incipient nucleation event becomes $E_1^* = \gamma_{usf}^{1,*} = \bar{\gamma}_{usf}^1 + \Delta\gamma_{usf}^1$, where $\Delta\gamma_{usf}^1$ is drawn from a Gaussian distribution using the mean and standard deviation obtained from sampling statistics. As shown in Figure 2a, this distribution of process barriers is then mapped as local values in the kMC mesh using the same dimensions from MS sampling (i.e., $\sqrt[3]{10} b_{112}$ by $\sqrt[3]{10} b_{112}$). As previously

discussed, this discretization also encompasses the region that contributes most significantly to excess energies during shearing (about 2-3 {111} planes, see Section 2.1). For mapping purposes, we assume that the critical planar fault energies have perfect statistical correlation at the same location in the kMC mesh but are otherwise spatially uncorrelated. That is, the same standard scores (i.e., the z-scores of the statistical distribution) are used when assigning critical planar fault energies to each location in the kMC mesh, but the spatial arrangement of standard scores within a specific critical planar fault energy is selected at random. This assumption finds some support with the statistical correlations measured in MS sampling, which were generally higher than 0.6 between all critical planar fault energy distributions. To capture the deformation twinning microstructure evolution, the deformation twinning fraction (F) and number of faults (N_F) are measured at each simulation along the $y = 0$ boundary of the simulation cell. In these calculations, ISFs, ESFs, and TFs are all counted towards F and N_F and the terms fault and twin will be used interchangeably. The simulation termination condition is set at a deformation twinning fraction of 0.15, which is in the range of experimental reports (i.e., 0.15 – 0.20, as per De Cooman et al.).²¹

2.3 Analytical Model

To reveal the relationship between the statistical parameters of critical planar fault energy distributions and the emergent deformation twinning microstructures, we develop an analytical model to predict the competition between deformation twin nucleation and thickening. As demonstrated in our previous work,⁹ in kMC simulations the ratio between the rate of change of fault number and deformation twinning fraction ($\frac{dN_F}{dF}$) is related to the probability of nucleation (P_N) through the evolution law:

$$\frac{dN_F}{dF} = NP_N \quad (4)$$

where N is the total number of {111} planes in the system. P_N is determined by the ratio between

rate of new twin nucleation (R_N) to the total rates of all kinetic events (R). Assuming glide events are exhausted, the total rate of all kinetic events is simply $R = R_N + R_T$, where R_T is the rate of twin thickening. By summing these rates at all nucleation sites, P_N is given by the following relationship:

$$P_N = \frac{\sum_{j1} \tilde{E}_1}{\sum_{j1} \tilde{E}_1 + \sum_{j\infty} \tilde{E}_\infty} \quad (5)$$

where $\tilde{E}_1 = \exp\{-aE_1(0, j1)\}$, $\tilde{E}_\infty = \exp\{-aE_\infty(0, j\infty)\}$, and $a = \frac{V\pi}{k_b T b_{112}}$, which holds the thermodynamic parameters. Here the indices $j1$ and $j\infty$ enumerate the $\{111\}$ slip planes in the kMC system where deformation twin nucleation and thickening can be activated, respectively. In the homogeneous model, where $E_k(0, j) = \bar{E}_k$, Eqs. (4) and (5) reduce to the following relation:⁹

$$\frac{dN_F}{dF} - N \left\{ \frac{(N - FN - 2N_F)\tilde{E}_1}{(N - FN - 2N_F)\tilde{E}_1 + 2N_F\tilde{E}_\infty} \right\} = 0 \quad (6)$$

which can be solved numerically using the 4th order Runge-Kutta method. As in our previous study,⁹ the number of nucleation sites available at a given deformation twinning fraction is taken as $N - FN - 2N_F$ and the number of thickening sites is $2N_F$. This treatment represents an upper bound for thickening sites and is most accurate at lower deformation twinning fractions.

For treatment of the heterogeneous model (i.e., $E_k(0, j) = E_k^*$), we extend this analytical derivation to incorporate the local statistical fluctuations in the GPFE landscape of solid solutions by considering the expected values of process rates (i.e., $\langle \exp\{-aE_k\} \rangle$). For simplicity of presentation, we have omitted the trailing (i, j) indices in the subsequent discussion. This derivation is based upon two assumptions: the distribution of process barriers follows Gaussian statistics (see Section 3.1) and that negative values of process barriers are not permitted. Although negative process barriers were not observed in the kMC mesh, in this model the tail of the associated Gaussian distribution can contain small, but non-zero probabilities of $E_k < 0$, which

leads to instability in the analysis. Consequently, distribution tails with negative values are set to zero in analytical modeling. This simplification limits the maximum rate of kMC processes to the Debye frequency, which aligns with Cai et al.⁷³ Under these assumptions, the expected value of the raised process barrier distribution $\langle \exp\{-aE_k\} \rangle$ is determined as:

$$\langle \exp\{-aE_k\} \rangle = \frac{1}{\sigma_k \sqrt{2\pi}} \left(\int_0^\infty \exp\{-aE_k\} \exp\left\{-\frac{1}{2} \left(\frac{E_k - \bar{E}_k}{\sigma_k} \right)^2\right\} dE_k \right. \quad (7a)$$

$$\left. + \int_{-\infty}^0 \exp\left\{-\frac{1}{2} \left(\frac{E_k - \bar{E}_k}{\sigma_k} \right)^2\right\} dE_k \right) \\ = \exp\left\{-a \left(\bar{E}_k - \frac{a\sigma_k^2}{2} \right)\right\} \left(\frac{1}{2} + \operatorname{erf}\left(\frac{\bar{E}_k - a\sigma_k^2}{\sqrt{2}\sigma_k} \right)/2 \right) + \left(\frac{1}{2} - \operatorname{erf}\left(\frac{\bar{E}_k}{\sqrt{2}\sigma_k} \right)/2 \right) \quad (7b)$$

where σ_k is the standard deviation of the k^{th} process barrier and erf is the error function. In Eq. (7b), the first exponential term represents the expected value of $\exp\{-aE_k\}$ over the full integration range (i.e., $-\infty$ to ∞) and the bracketed terms with the error functions are correction factors to account for treatment of the distribution tail that falls below zero. An effective process barrier \hat{E}_k can now be defined by setting Eq. (7b) equal to an effective exponential term ($\exp\{-a\hat{E}_k\}$), which simplifies to the following relation:

$$\hat{E}_k = -\frac{1}{a} \ln \left[\exp\left\{-a \left(\bar{E}_k - \frac{a\sigma_k^2}{2} \right)\right\} \left(\frac{1}{2} + \operatorname{erf}\left(\frac{\bar{E}_k - a\sigma_k^2}{\sqrt{2}\sigma_k} \right)/2 \right) \right. \quad (8) \\ \left. + \left(\frac{1}{2} - \operatorname{erf}\left(\frac{\bar{E}_k}{\sqrt{2}\sigma_k} \right)/2 \right) \right]$$

Examination of the extremes Eq. (8) shows that \hat{E}_k converges to \bar{E}_k as $\sigma_k \rightarrow 0$, as expected, and $\hat{E}_k \rightarrow -\frac{1}{a} \ln \left(\frac{1}{2} \right) \approx 0$ as $\sigma_k \rightarrow \infty$. The residual term in the latter limit arises due to the elimination of the negative portion of the distribution tail in this derivation. Given Eq. (8), Eq. (6) may now be solved for the heterogeneous model using the same numerical methods by inserting the

appropriate effective process barriers (i.e., $E_1(0, j) = \hat{E}_1$ and $E_\infty(0, j) = \hat{E}_\infty$).

The final consideration in this analytical model is the determination of the statistical parameters of the process barriers. The deformation twin nucleation barrier (i.e., E_1) is defined explicitly by the unstable stacking fault energy, which delivers $\bar{E}_1 = \bar{\gamma}_{usf}^1$ and $\sigma_1 = \sigma_{usf}^1$. However, as the deformation twin thickening barrier is defined by the difference of two correlated critical planar fault energies (i.e., $E_\infty \approx \gamma_{utf}^3 - 2\gamma_{tf}$), the statistical parameters become $\bar{E}_\infty = \bar{\gamma}_{utf}^3 - 2\bar{\gamma}_{tf}$ and $(\sigma_\infty)^2 = (\sigma_{utf}^3)^2 + (\sigma_{2tf})^2 - 2\sigma_{utf}^3\sigma_{2tf}corr(\gamma_{utf}^3, 2\gamma_{tf})$, where $corr(\gamma_{utf}^3, 2\gamma_{tf}) \approx 0.75$ is the statistical correlation coefficient between the unstable twinning fault and twinning fault energies measured in MS simulations.

2.4 Molecular dynamics simulations of nanowires in tension

The simplifications and assumptions undertaken to develop the kMC and analytical models motivate the search for an independent validation method. In this regard, MD nanowire tensile simulations offer several attractive features to verify the predictions of deformation twinning microstructures. Namely, the deformation of a nanowire proceeds from the nucleation of Shockley partial dislocations at free surfaces, and a sufficiently long nanowire therefore possesses a statistically representative collection of nucleation sites. Furthermore, the structural topology of free surface nucleation sites in MD are nearly identical. This aligns well with the conditions of kMC simulations, where the selective activation of deformation mechanisms relies only on the heterogeneities introduced by the chemical topology.

MD nanowire tensile testing is performed using LAMMPS. OVITO is used to visualize the atomic topologies in MD simulations and deformation twinning structures are identified using the Crystal Analysis Tool.⁷⁹ The same EAM potential used in Section 2.1 is implemented in MD simulations to model interatomic interactions. Although stacking faults and deformation twins are

commonly observed in nanowires,^{57,60} the competition between deformation twinning and other mechanisms (e.g., dislocation slip) is highly orientation dependent. To ensure activation of deformation twinning mechanisms only, nanowires are modeled with the $\langle 118 \rangle$, $\langle 1\bar{1}0 \rangle$, and $\langle 44\bar{1} \rangle$ crystallographic directions aligned to the global x , y , and z axes, respectively. This orientation maximizes Schmid factors along the $\langle 11\bar{2} \rangle / \{111\}$ twinning system. Nanowires are constructed with square cross-sections using a deletion scheme outlined in previous work.⁹ The dimensions of the nanowire are selected to align with the sizes of kMC simulations ($66b_{112}$ by $300d_{111}$), which results in nanowires measuring ~ 6 by 87 nm along the x and z axes, respectively. The nanowires are modeled at an equimolar NiCo composition and possess approximately 400,000 atoms, with solute randomly assigned to each atomic site. A size sensitivity analysis for the MD nanowire testing is provided in Section S4, Figure S4 of the Supplementary Materials. Periodic boundary conditions are enforced along all the axes, with a 6 nm vacuum layer in the x and y directions between periodic replications. A typical nanowire and the relationships between the twinning system, crystallographic and simulation axes are provided in Figure 3.

MD nanowire tensile simulations begin with static relaxation under the conjugate gradient energy minimization method. Subsequently, initial velocities are assigned to atoms by drawing values from a Gaussian distribution centered at a temperature of 300K. After velocity application, the nanowires are equilibrated using a Nosé-Hoover style thermostat and barostat, which maintains a stress-free loading on the system boundaries and a temperature of 300 K. Following equilibration, uniaxial tensile testing is achieved by strain-controlled deformation along the longitudinal axis of the nanowire at a strain rate of $10^9/\text{s}$. A time step of 1 fs is used for all simulations and testing is replicated 7 times.

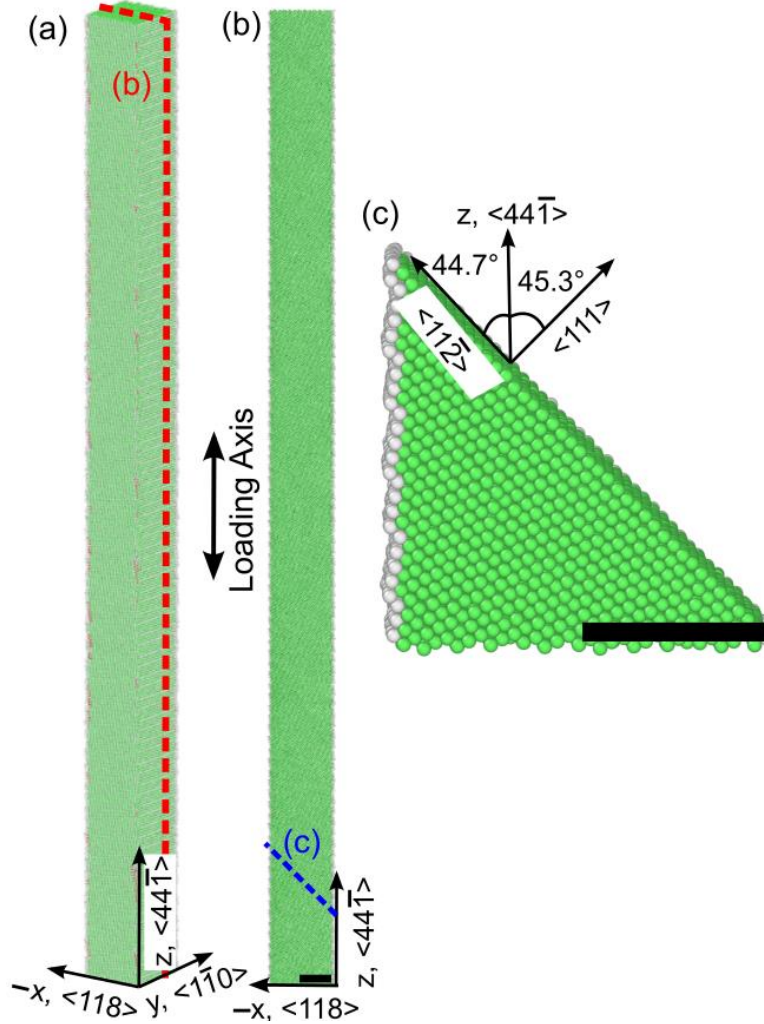


Figure 3: (a) A snapshot of a nanowire created for MD tensile testing simulations. (b) A planar section of the nanowire from (a) with the trace of a $\{111\}$ slip plane shown in dashed blue stroke. This slip-plane is oriented to maximize the Schmid factor along the $(11\bar{2})$ crystallographic direction. (c) A closeup of the nanowire with a slip-plane exposed. The angular relations between crystallographic and simulation axes are indicated. Scale bars in (b) and (c) measure 3 nm each. Atoms shown in green are FCC coordinated and white atoms do not have a fixed symmetry.

3. RESULTS AND DISCUSSION

The report of results begins with an analysis of the statistics collected from MS simulations. These statistics are then used to generate the process barriers for the homogeneous and heterogeneous kMC models using the methods described in Section 2.2. kMC simulation cells are constructed for equimolar NiCo samples and measure $66b_{112}$ by $300d_{111}$. The deformation twinning fraction and fault number density are measured at each kMC simulation timestep to track

the competition between nucleation and thickening processes. Each kMC simulation is replicated 200 times for statistical sampling, with results converging well below the replication limit. A sensitivity analysis of the kMC system size and replication number is provided in Sections S4 and S5 of the Supplementary Materials, respectively. We use the symbols $\overline{\text{NiCo}}$ and NiCo^* to denote results for the homogeneous and heterogeneous models, respectively. The results of kMC simulations are then examined using the analytical model of Section 2.3 and validated by MD nanowire tensile simulations. All error is reported as ± 1 standard deviation.

3.1 Statistics of the GPFE landscape

Figure 4 provides the results of MS sampling of equimolar NiCo samples. As shown in Figure 4a, significant deviations from the nominal equimolar chemistry are observed during local sampling. The sampling data is reported here as a binned histogram, which has been overlaid with a fitted probability density function (PDF). The local samples are found to exhibit a Gaussian distribution ($\approx 0.50 \pm 0.08$) about the mean molar value, as anticipated. A slight asymmetry in the distribution creates small deviations from the nominal equimolar value (i.e., 0.50), but these deviations are less than 0.01 by mole. Although these variations in chemistry are sensitive to sampling dimensions, they are reported here to underscore the link between fluctuations in the GPFE landscape and local composition.

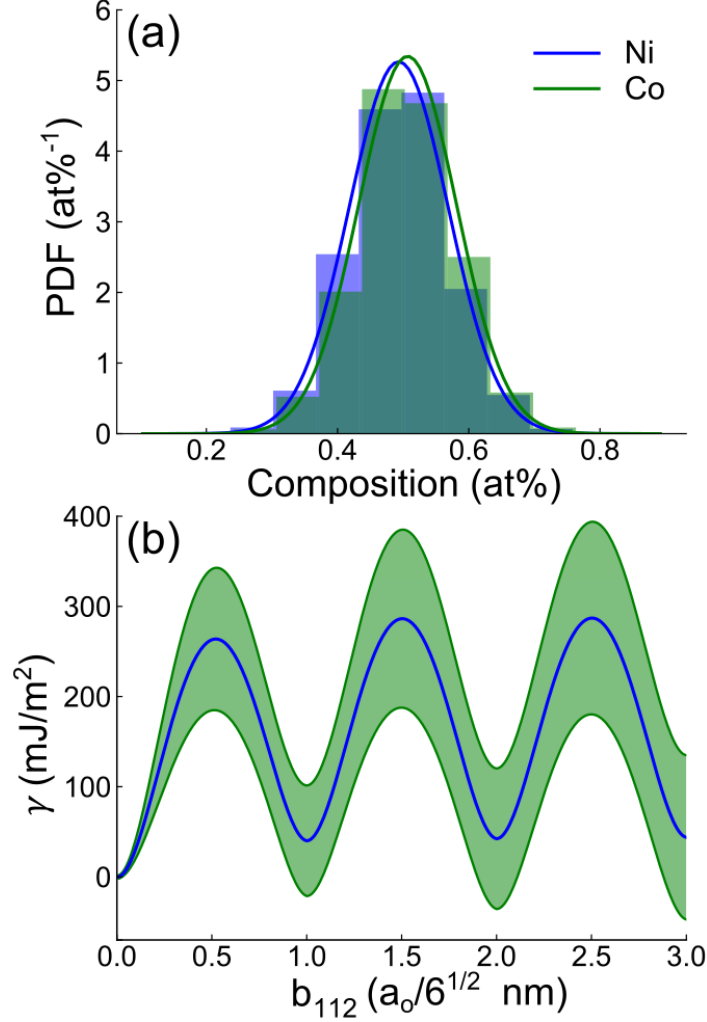


Figure 4: (a) A histogram showing the composition statistics measured during local sampling of the GPFE landscape. The probability density function (PDF) is fit to the collected samples. The values for composition are shown in atomic percent (i.e., by mole). (b) The fluctuations in the GPFE landscape are shown for the local sampling of equimolar NiCo samples. The green region provides the bounds of ± 1 standard deviation for the measured planar fault energies (average shown in blue stroke).

The results of local sampling of the GPFE landscape are provided in Figure 4b. Here, the blue lines provide the average data and the green region represents the ± 1 standard deviation from the mean. It should be noted that the average of the locally-sampled GPFE landscape data aligns well with the GPFE landscape calculated over the entire system area, as expected. Furthermore, the statistical fluctuations in the GPFE landscape are independent of sampling dimension along $\langle 111 \rangle$, as per the excess energy arguments presented in Section 2.1. Examination of the statistical scatter in the GPFE landscape highlights the dramatic variations in fault energies that are encountered

locally along the planar defect. As shown in Section S3, Figure S3 of the Supplementary Materials, the statistical scatter in the GPFE landscape vanishes as the sample area (i.e., in the $\{111\}$ plane) approaches the system size. One interesting observation is that the stable fault energies (i.e., γ_{isf} , γ_{esf} , and γ_{tf}) exhibit negative values in some samples, which aligns with recent reports in the literature. For instance, NiCo is known to undergo an FCC to hexagonal close-packed (HCP) transformation at chemistries of > 70 at.% Co,⁸⁰ which implies a negative intrinsic stacking fault energy for these Co-rich compositions. Indeed, negative stacking fault energies have been reported in NiCo⁴¹ and NiCo-based MEA^{30,40,42} systems in DFT studies, which is related, in part, to limitations in the simulation cell size available to first principles methods.^{46,48} Within this context, we interpret negative stacking fault energies in this study as arising from Co-rich regions localized within the fault plane.

Figure 5 provides the distributions of critical planar fault energies obtained from local sampling of the GPFE landscape. As shown in the figure, the binned data is overlaid with a fitted Gaussian distribution. The statistical parameters of the critical planar fault energy distributions have been provided in the plot and are summarized in Table II. Each critical planar fault energy distribution is found to be reasonably approximated by a Gaussian with minor skewing noted in the unstable stacking fault energy (i.e., γ_{usf}^1). These results align with a study from Zhao et al.⁴⁶ who report a normal distribution of intrinsic stacking fault energies for several concentrated FCC solid solutions. The data provided in Figure 5 also emphasizes the proportion of negative stable fault energies, which appears to be almost half of the distribution for each fault type. It should be noted that the twinning fault energy (i.e., γ_{tf}) is doubled as two twin faults are created by MS shearing operations. Furthermore, the standard deviation (i.e., σ_{2tf}) is provided in reference to the $2\gamma_{tf}$ distribution. Collectively, the statistical distributions reported here underscore the large variations

in processes barriers encountered by dislocations during the operation of deformation twinning. In the subsequent section, the statistical parameters obtained from Gaussian fitting of the critical planar fault energy distributions are leveraged to inform kMC process barriers, through which the effects on the evolution of deformation twinning microstructures are examined.

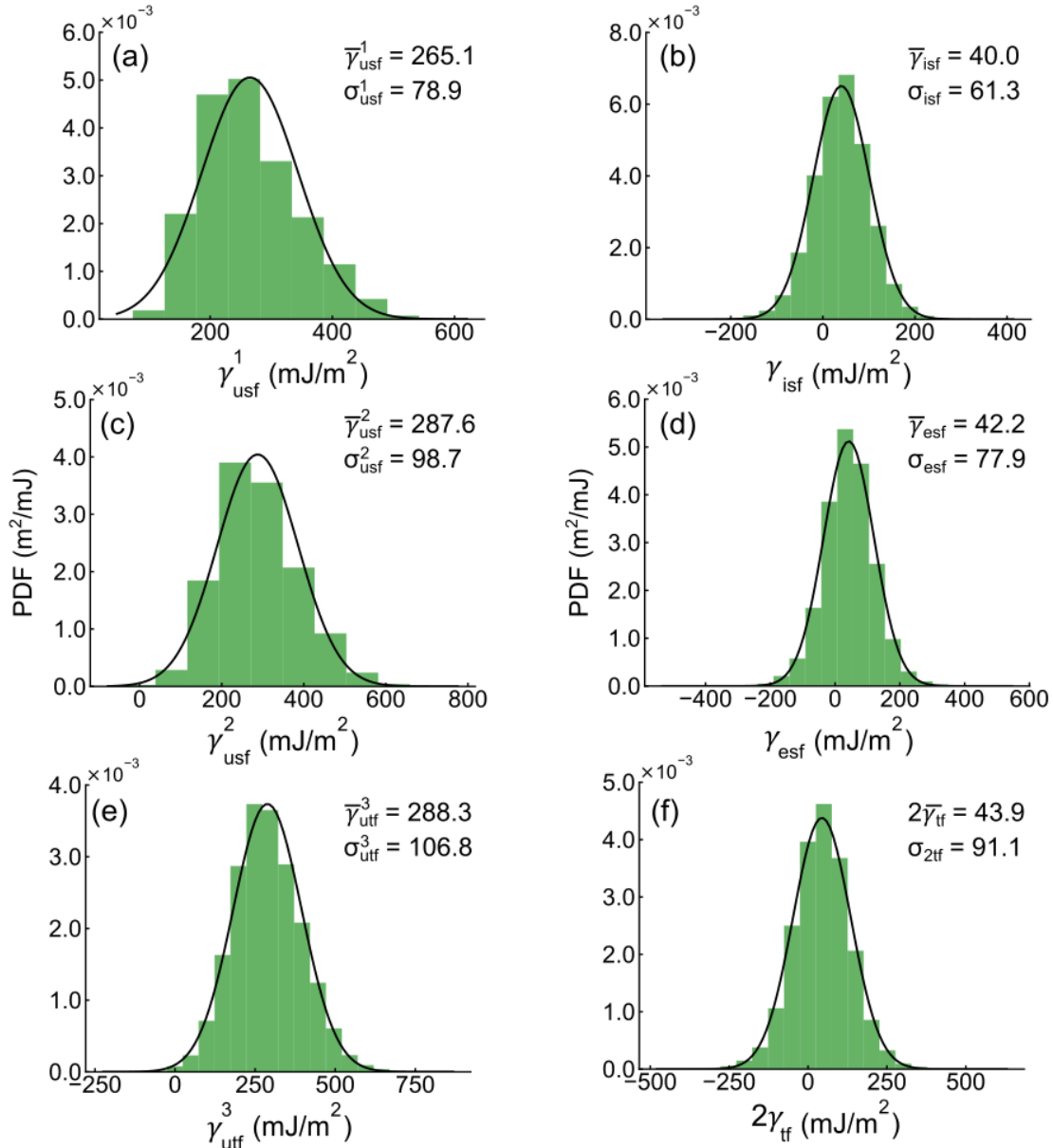


Figure 5: The distribution of critical planar fault energies sampled from the GPFE landscape of equimolar NiCo, shown as histograms. The unstable planar fault energies sampled are the (a,c) unstable stacking and (e) unstable twinning fault energies (i.e., γ_{usf}^1 , γ_{usf}^2 , and γ_{utf}^3). The stable fault energies sampled are the (b) intrinsic and (d) extrinsic stacking fault and (f) twinning fault energies (i.e., γ_{isf} , γ_{esf} , and γ_{tf}). A Gaussian fit to the histogram data is overlaid and the statistical parameters are provided (i.e., the average and standard deviation). The stable twinning fault energy is provided at double its value as there are two twin faults created during MS shearing operations.

Table II: Average and standard deviations of critical planar fault energies (mJ/m²) as measured from MS simulations.

Model	$\bar{\gamma}_{usf}^1 \pm \sigma_{usf}^1$	$\bar{\gamma}_{usf}^2 \pm \sigma_{usf}^2$	$\bar{\gamma}_{utf}^3 \pm \sigma_{utf}^3$	$\bar{\gamma}_{isf} \pm \sigma_{isf}$	$\bar{\gamma}_{esf} \pm \sigma_{esf}$	$2\bar{\gamma}_{tf} \pm \sigma_{2tf}$
NiCo*	265.1±78.9	287.6±98.7	288.3±106.8	40.0±61.3	42.2±77.9	43.9±91.1
NiCo	265.1	287.6	288.3	40.0	42.2	43.9

3.2 Evolution of deformation twinning microstructures

Representative snapshots of the microstructure of the kMC simulation cell are provided in Figure 6a and Figure 6b for the homogeneous and heterogeneous models, respectively. The colored regions represent areas that are faulted and/or twinned in the microstructure. The evolution of deformation twinning microstructures shows distinct behaviors between the two models. In the homogeneous system, the fault number density is comparatively lower and is accompanied by thicker deformation twins at each twinning fraction. By contrast, the heterogeneous system is profusely twinned, with most defects appearing as one- and two-layer stacking faults (i.e., ISFs and ESFs). One observation from this result is that the presence of a variable process barrier landscape disproportionately biases deformation twinning towards nucleation mechanisms. This interpretation aligns with the correlations between process barrier statistics, as discussed in Section 2.3. Specifically, the larger standard deviations in the nucleation barrier compensate for its higher relative average value (i.e., $E_1 = 265.1 \pm 78.9$ mJ/m²), which drives nucleation-dominated deformation behavior. Conversely the process barriers to thickening, exhibit lower standard deviations due to correlations between critical planar fault energies that reduce the statistical scatter (e.g., $E_\infty = 244.4 \pm 71.2$ mJ/m²).

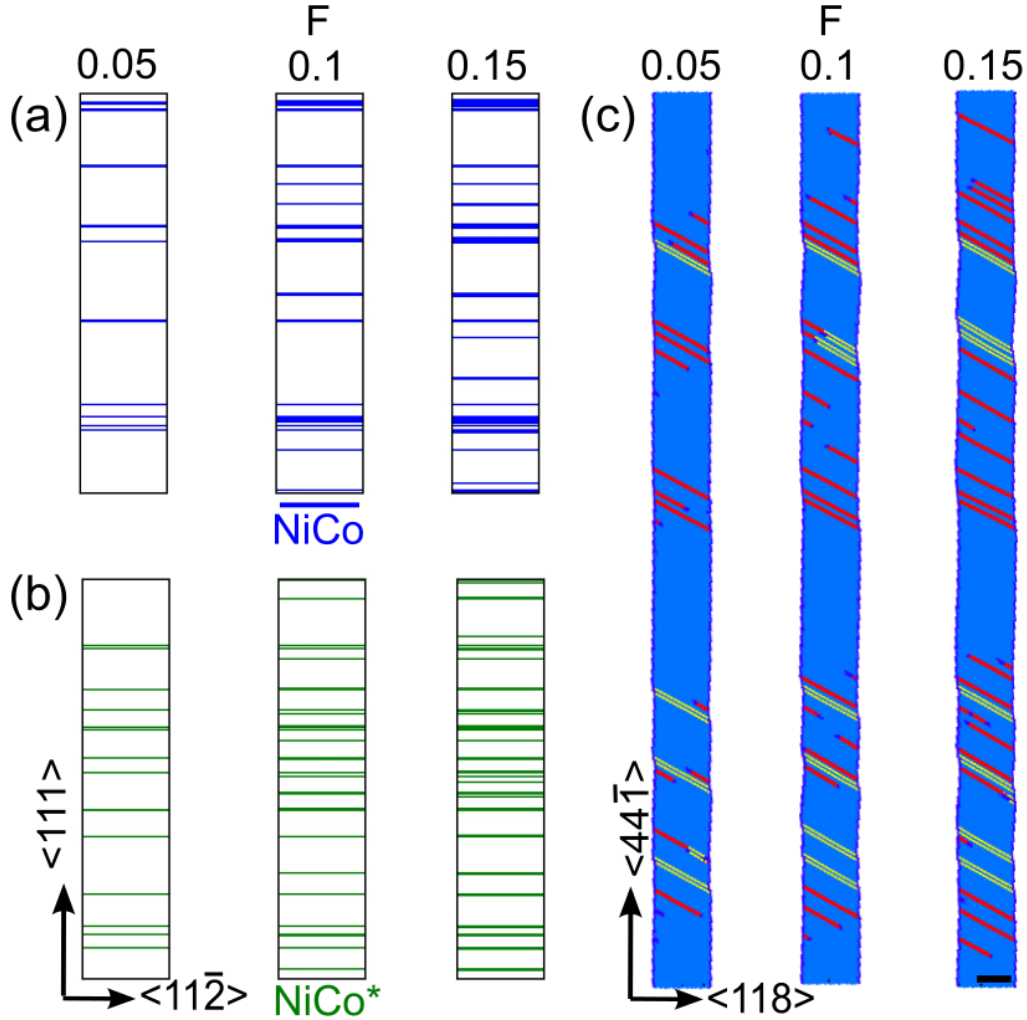


Figure 6: Representative snapshots from (a,b) kMC and (c) MD nanowire tensile simulations at deformation twinning fractions of 0.05, 0.1, and 0.15. For the heterogeneous NiCo model (green), the simulation is segmented by several planar defects that traverse across the cell. For the homogeneous NiCo model (blue), the snapshots reveal a lower density of planar defects with larger average thicknesses. MD snapshots are taken from the center cross-section of a representative nanowire and show fault-free FCC atoms (blue), ISFs (red), ESFs/TFs (yellow) and atoms without a fixed symmetry (dark blue). The scalebar in (c) measures 3 nm.

Snapshots of representative defect structures during MD nanowire tensile testing are provided in Figure 6c. Here, planar defects are shown in red and yellow stroke for ISFs and ESFs/TFs, respectively. The deformation twinning fractions are calculated using an image processing algorithm described in our previous work.⁹ As shown in the image, nanowire samples exhibit a monotonic increase in planar faults with increasing deformation twinning fraction. Activation of dislocation slip is not observed in the deformation of MD nanowires, as expected from Schmid

theory. The deformation twinning microstructures of the MD nanowires are qualitatively similar to those of the heterogeneous model in number density and thickness. A quantitative comparison of kMC and MD results follows in the subsequent discussion.

Figure 7 provides the evolution of the fault number density for each of the methods examined in this effort. The fault number density is defined here as $n_F = N_F / Nd_{111}$ and has been computed by considering contributions from planar faults (i.e., ISFs and ESFs) and thickened TFs, as previously discussed. The results of kMC simulations for both the heterogeneous and homogeneous models are provided as averages with error bars indicating 1 standard deviation over 200 replications. As shown in the figure, the differences between the heterogeneous and homogeneous kMC models are quantitatively consistent with the qualitative observations from the snapshots of deformation provided in Figure 6. That is, deformation twinning processes in the heterogeneous model favor nucleation relative to the homogeneous simulations. The evolution of the fault number density in MD nanowire tensile simulations is overlaid with the kMC data in red stroke. Here, the average data is represented by the red midline and ± 1 standard deviation is given by the bounds of the shaded area. Examination of the MD data shows excellent agreement with the heterogeneous model. This outcome is significant and offers two key observations. First, as an independent predictor of deformation twinning physics, the agreement of MD results with kMC methods provides encouraging validation of our approach. Second, the alignment of MD results specifically with the heterogeneous kMC model underscores the influence of variable process barriers on the activation of deformation twinning processes in FCC solid solutions.

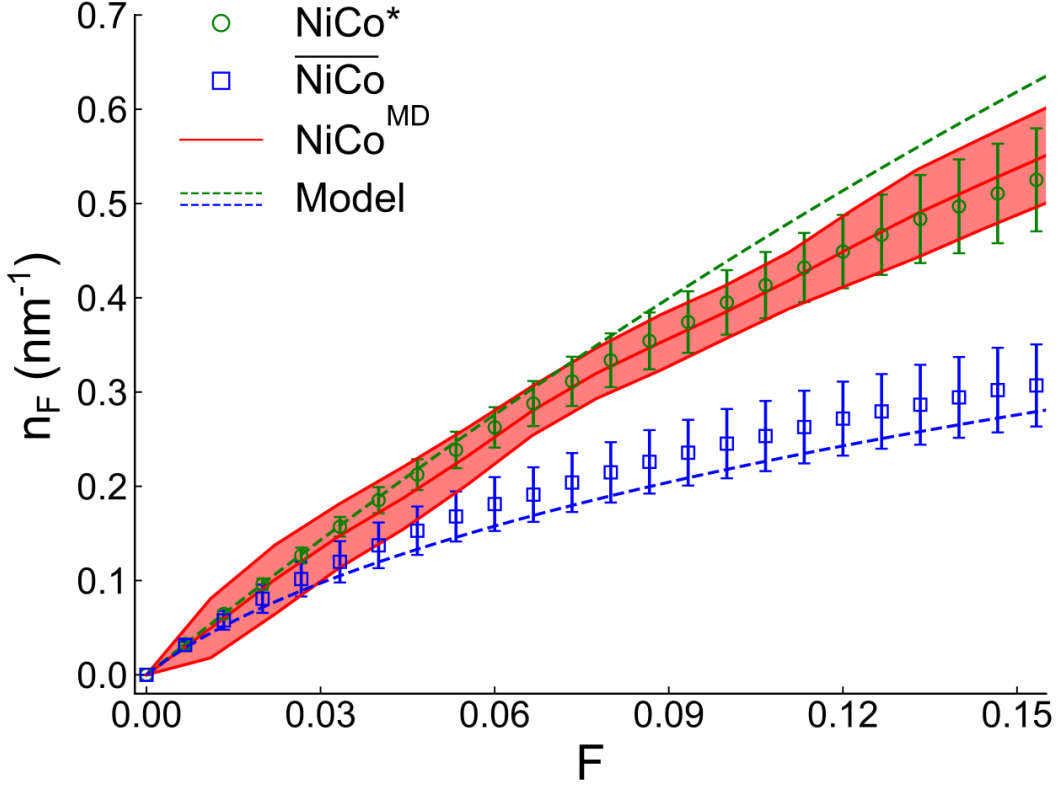


Figure 7: The evolution of the fault number density as predicted by heterogeneous (green) and homogeneous (blue) kMC models and MD simulations (red, NiCo^{MD}). The average kMC results over 200 replications are provided, and error bars represent ± 1 standard deviation. The average of MD results is provided by the solid midline and the shaded region represents the bounds of 1 standard deviation. These results are overlaid with numerical solutions to analytical model for the homogeneous (blue dashed line) and the heterogeneous (green dashed lines) calculations, as determined using the relevant process barriers.

Numerical solutions to the analytical model developed in Section 2.3 are provided for the homogeneous and heterogeneous systems in Figure 7. In the homogeneous solution, the fault number density is calculated from the solution of Eq. (6) using the average values of the process barriers (i.e., $E_1 = 265.1 \text{ mJ/m}^2$ and $E_\infty = 244.4 \text{ mJ/m}^2$). However, for the heterogeneous solution, computation of Eq. (6) proceeds using the effective process barriers (i.e., \hat{E}_1 and \hat{E}_∞) that are determined from Eq. (8) with $\bar{E}_1 = 265.1 \text{ mJ/m}^2$, $\sigma_1 = 78.9 \text{ mJ/m}^2$, $\bar{E}_\infty = 244.4 \text{ mJ/m}^2$, and $\sigma_\infty = 71.2 \text{ mJ/m}^2$. In both analytical calculations, the other model parameters match those used in kMC simulations. As shown in the figure, the analytical model is in good agreement with the results of kMC and MD simulations. Some over-prediction at high deformation twinning fractions is noted in the heterogeneous analytical calculations, which may be due to merging of planar defect

structures in highly twinned microstructures, as described in previous work.⁹ Nonetheless, a key observation from analytical modeling is that the essential physics of deformation twin nucleation and thickening in solid solutions can be captured through consideration of statistical fluctuations in the relevant process barriers. This outcome supports scalability of the analysis to larger system sizes without the significant computational overhead incurred by kMC and MD simulations.

Although the fault number density predictions find excellent agreement with MD nanowire tensile simulations in this work and in our previous study,⁹ this alignment must be interpreted with caution. Namely, dislocation nucleation and glide kinetics are known to have significant nonlinearities under the high strain rate loadings imposed by MD simulations. These include nonlinear contributions of applied stresses to activation barrier kinetics and variable activation volumes.^{58,81} Therefore, MD nanowire tensile simulations at different temperatures or strain rates may require different activation parameters (e.g., activation volumes) to be used to find agreement with kMC and analytical predictions. Nonetheless, we emphasize that this combination of thermomechanical testing parameters (i.e., 300 K temperature and $10^9/\text{s}$ strain rate) is consistent with the kMC and analytical model across several FCC systems, as shown here and in previous work.⁹ As an additional note, MD testing under different temperatures and strain rates may activate different dislocation-mediated mechanisms (e.g., as in Refs.^{82–84}) that are not directly captured by kMC or analytical models, but we expect this is largely precluded by the nanowire and loading configurations used in this study.

3.3 Competition between nucleation and thickening processes in FCC solid solutions

The presentation of the analytical model for the fault number density evolution motivates a broader examination of the competition between the nucleation and thickening processes of deformation twinning in solid solutions. In our previous work,⁹ we developed a twin nucleation

tendency criterion (T_η) for a similar purpose in unary FCC systems. Using the definition of the effective barrier from Eq. (8), T_η may be updated to incorporate the statistics of variable GPFE landscapes in FCC solid solutions as:

$$T_\eta = \ln\left(\frac{1 - F - 2n_F d_{111}}{2n_F d_{111}}\right) - a(\hat{E}_1 - \hat{E}_\infty) \quad (9)$$

where the nucleation of deformation twins is favored when $T_\eta > 0$ and the thickening of existing deformation twins is preferred when $T_\eta < 0$. The first term in T_η captures the changes in nucleation and thickening tendencies based on the evolution of deformation twinning microstructures. That is, as the fault number density rises, fewer sites become available for nucleation of new defects and thickening becomes increasingly favored. The second term in T_η accounts for contributions of the process barriers to the inherent competition between nucleation and thickening processes. Figure 8 plots the evolution of T_η with increasing deformation twinning fraction for both the homogeneous and heterogeneous models. As shown in the figure, both models exhibit a monotonic decline in nucleation-favored behavior at increasing deformation twin fractions, as expected with the microstructure becoming increasingly faulted. Furthermore, the heterogeneous model is observed to favor nucleation of deformation twins relative to the homogeneous model, which is consistent with the results presented in the kMC analysis. This finding further underscores the sensitivity of deformation twinning mechanisms to the statistical fluctuations in process barriers. In order to study the effects of length-scale on the twin nucleation tendency, we have also plotted T_η for varied GPFE landscape sampling areas, which presents the opportunity to examine the twin nucleation tendency under process barriers with varied statistical scatter. As shown in the figure, the twin nucleation tendency criterion converges to the homogeneous limit at a sampling area of $25A^*$. This result is significant as it reveals the length-scale over which the influence of statistical

fluctuations in process barriers diminish and the local behavior transitions towards the bulk.

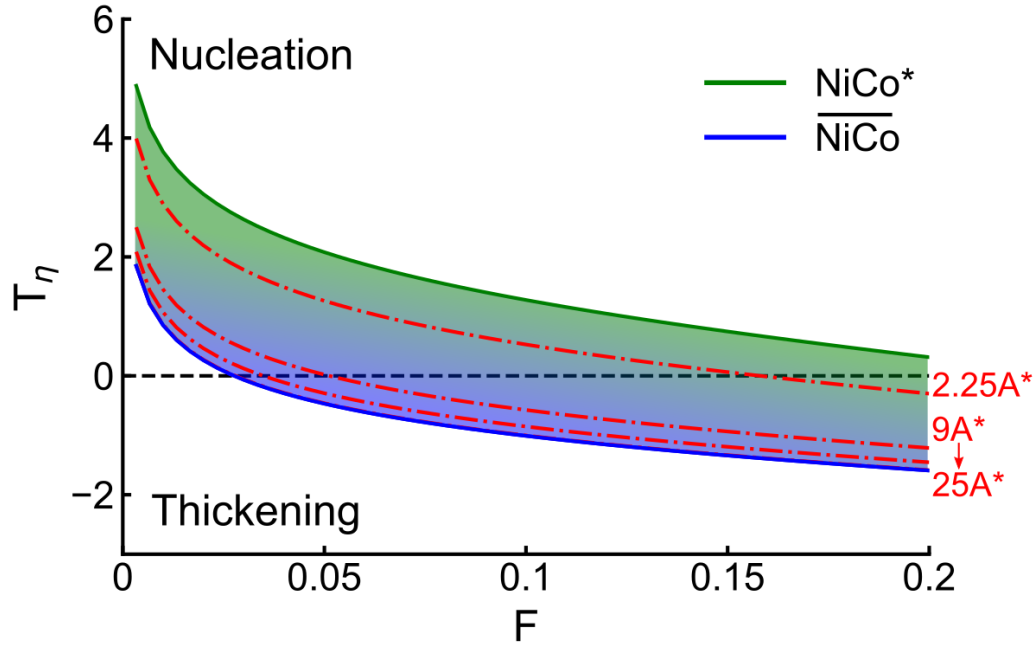


Figure 8: The evolution of the twin nucleation tendency criterion. The nucleation of deformation twins is preferred when $T_\eta > 0$ and thickening-favored behavior is expected when $T_\eta < 0$. The data is plotted for the homogeneous and heterogenous models in blue and green stroke, respectively. The sampling area used to define the statistics of process barriers is varied between $2.25A^*$ and $25A^*$, with criterion predictions converging to the homogeneous values at larger sampling areas.

4. CONCLUSIONS

The effects of local fluctuations in planar fault energies on the deformation twinning microstructures of FCC solid solutions have been examined by kMC simulations, with equimolar NiCo serving as the benchmark system. To examine the evolution of deformation twinning microstructures, the processes of nucleation and thickening of deformation twins were of specific interest in kMC simulations. The fluctuating process barriers for activation of nucleation and thickening behaviors were assigned using statistical parameters obtained from local sampling of the GPFE landscape. kMC results showed an increase in the fault number densities in NiCo solid solution samples when compared against a homogenized reference calculation where statistical scatter was not considered. Furthermore, the results of kMC simulations were compared with MD nanowire tensile simulations, which showed excellent agreement with the NiCo solid solution

samples. This alignment served to independently validate our kMC approach and underscored the importance of local fluctuations in driving deformation twinning behaviors.

In addition to kMC studies, an analytical model was developed to predict the evolution of the fault number density in FCC solid solutions using the process barriers of deformation twinning as key inputs. To capture the effects of fluctuations, a relation for an effective barrier was derived, which was based on the expected values of deformation twinning kinetics under a statistical distribution of process barriers. The formulation of this analytical model enabled a direct analysis of the competition between nucleation- and thickening-favored deformation twinning processes. In addition, this model revealed the length-scale by which the effects of local fluctuations on the deformation twinning processes diminish and the nucleation/thickening-dominated behaviors converge to bulk predictions. More broadly, the tools developed in this work provide a pathway to study the influence of chemistry and length-scale on the evolution of deformation twinning mechanisms in FCC solid solutions.

SUPPLEMENTARY MATERIAL

Supplementary material is available in the online version of the paper or by email request from the corresponding author (mattdaly@uic.edu).

ACKNOWLEDGEMENTS

This material is based upon work supported by the National Science Foundation under Grant No. DMR-2144451. The authors gratefully acknowledge the Advanced Cyberinfrastructure for Education and Research (ACER) group at the University of Illinois at Chicago for providing the computational resources and services needed to deliver the research results delivered within this paper. URL: <https://acer.uic.edu>. The authors would also like to thank Amir Shirsalimian for his comments on this manuscript.

AUTHOR DECLARATIONS

Conflicts of Interest

The authors declare no conflict of interest.

Author Contributions

Ritesh Jagatramka: formal analysis (lead), investigation (lead), methodology (equal), software (lead), validation (lead), visualization (lead) writing – original draft (equal), writing – review and editing (equal). **Junaid Ahmed:** formal analysis (supporting), investigation (supporting), software (supporting). **Matthew Daly:** conceptualization (lead), formal analysis (supporting), funding acquisition (lead), investigation (supporting), methodology (equal), project administration (lead), resources (lead), supervision (lead), visualization (supporting), writing – original draft (equal), writing – review and editing (equal)

DATA AVAILABILITY

The data that support the findings of this study are available from the corresponding author upon reasonable request.

REFERENCES

- ¹ V. Vitek, Philos. Mag. **18**, 773 (1968).
- ² V. Vitek, Scr. Metall. **4**, 725 (1970).
- ³ J.R. Rice, J. Mech. Phys. Solids **40**, 239 (1992).
- ⁴ S. Ogata, J. Li, and S. Yip, Phys. Rev. B **71**, 224102 (2005).
- ⁵ E.B. Tadmor and S. Hai, J. Mech. Phys. Solids **51**, 765 (2003).
- ⁶ E.B. Tadmor and N. Bernstein, J. Mech. Phys. Solids **52**, 2507 (2004).
- ⁷ R.J. Asaro and S. Suresh, Acta Mater. **53**, 3369 (2005).
- ⁸ R. Jagatramka and M. Daly, JOM **74**, 3799 (2022).

- ⁹ M. Daly, A. Kumar, C.V. Singh, and G. Hibbard, *Int. J. Plast.* **130**, 102702 (2020).
- ¹⁰ O. Grässel, G. Frommeyer, C. Derder, and H. Hofmann, *Le J. Phys. IV* **07**, C5 (1997).
- ¹¹ O. Grässel, L. Krüger, G. Frommeyer, and L.. W. Meyer, *Int. J. Plast.* **16**, 1391 (2000).
- ¹² O. Bouaziz and N. Guelton, *Mater. Sci. Eng. A* **319–321**, 246 (2001).
- ¹³ S. Allain, J.-P. Chateau, O. Bouaziz, S. Migot, and N. Guelton, *Mater. Sci. Eng. A* **387–389**, 158 (2004).
- ¹⁴ S. Allain, J.-P. Chateau, and O. Bouaziz, *Mater. Sci. Eng. A* **387–389**, 143 (2004).
- ¹⁵ O. Bouaziz, S. Allain, and C. Scott, *Scr. Mater.* **58**, 484 (2008).
- ¹⁶ O. Bouaziz, S. Allain, C.P. Scott, P. Cugy, and D. Barbier, *Curr. Opin. Solid State Mater. Sci.* **15**, 141 (2011).
- ¹⁷ O. Bouaziz, *Scr. Mater.* **66**, 982 (2012).
- ¹⁸ O. Bouaziz, D. Barbier, J.D. Embury, and G. Badinier, *Philos. Mag.* **93**, 247 (2013).
- ¹⁹ D.R. Steinmetz, T. Jäpel, B. Wietbrock, P. Eisenlohr, I. Gutierrez-Urrutia, A. Saeed–Akbari, T. Hickel, F. Roters, and D. Raabe, *Acta Mater.* **61**, 494 (2013).
- ²⁰ B.C. De Cooman, O. Kwon, and K.-G. Chin, *Mater. Sci. Technol.* **28**, 513 (2012).
- ²¹ B.C. De Cooman, Y. Estrin, and S.K. Kim, *Acta Mater.* **142**, 283 (2018).
- ²² F. Otto, A. Dlouhý, C. Somsen, H. Bei, G. Eggeler, and E.P. George, *Acta Mater.* **61**, 5743 (2013).
- ²³ J. Antonaglia, X. Xie, Z. Tang, C.-W. Tsai, J.W. Qiao, Y. Zhang, M.O. Laktionova, E.D. Tabachnikova, J.W. Yeh, O.N. Senkov, M.C. Gao, J.T. Uhl, P.K. Liaw, and K.A. Dahmen, *JOM* **66**, 2002 (2014).
- ²⁴ B. Gludovatz, A. Hohenwarter, D. Catoor, E.H. Chang, E.P. George, and R.O. Ritchie, *Science* (80-.). **345**, 1153 (2014).

- ²⁵ W. Abuzaid and H. Sehitoglu, *Mater. Charact.* **129**, 288 (2017).
- ²⁶ S. Alkan, A. Ojha, and H. Sehitoglu, *Acta Mater.* **147**, 149 (2018).
- ²⁷ A.S. Tirunilai, T. Hanemann, C. Reinhart, V. Tschan, K.-P. Weiss, G. Laplanche, J. Freudenberger, M. Heilmaier, and A. Kauffmann, *Mater. Sci. Eng. A* **783**, 139290 (2020).
- ²⁸ X. Wu, M. Yang, P. Jiang, C. Wang, L. Zhou, F. Yuan, and E. Ma, *Scr. Mater.* **178**, 452 (2020).
- ²⁹ Y. Ma, F. Yuan, M. Yang, P. Jiang, E. Ma, and X. Wu, *Acta Mater.* **148**, 407 (2018).
- ³⁰ Z.Z. Zhang, H. Sheng, Z. Wang, B. Gludovatz, Z.Z. Zhang, E.P. George, Q. Yu, S.X. Mao, and R.O. Ritchie, *Nat. Commun.* **8**, 14390 (2017).
- ³¹ S. Huang, H. Huang, W. Li, D. Kim, S. Lu, X. Li, E. Holmström, S.K. Kwon, and L. Vitos, *Nat. Commun.* **9**, 2381 (2018).
- ³² Z. Li, K.G. Pradeep, Y. Deng, D. Raabe, and C.C. Tasan, *Nature* **534**, 227 (2016).
- ³³ Y. Deng, C.C. Tasan, K.G. Pradeep, H. Springer, A. Kostka, and D. Raabe, *Acta Mater.* **94**, 124 (2015).
- ³⁴ N. Stepanov, M. Tikhonovsky, N. Yurchenko, D. Zyabkin, M. Klimova, S. Zherebtsov, A. Efimov, and G. Salishchev, *Intermetallics* **59**, 8 (2015).
- ³⁵ M. Klimova, N. Stepanov, D. Shaysultanov, R. Chernichenko, N. Yurchenko, V. Sanin, and S. Zherebtsov, *Materials (Basel)*. **11**, 53 (2017).
- ³⁶ Z. Li, S. Zhao, R.O. Ritchie, and M.A. Meyers, *Prog. Mater. Sci.* **102**, 296 (2019).
- ³⁷ A.J. Zaddach, C. Niu, C.C. Koch, and D.L. Irving, *JOM* **65**, 1780 (2013).
- ³⁸ Z.H. Jin, S.T. Dunham, H. Gleiter, H. Hahn, and P. Gumbsch, *Scr. Mater.* **64**, 605 (2011).
- ³⁹ B.P. Eftink, N.A. Mara, O.T. Kingstedt, D.J. Safarik, J. Lambros, and I.M. Robertson, *Mater. Sci. Eng. A* **618**, 254 (2014).
- ⁴⁰ J. Ding, Q. Yu, M. Asta, and R.O. Ritchie, *Proc. Natl. Acad. Sci.* **115**, 8919 (2018).

- ⁴¹ S. Zhao, G.M. Stocks, and Y. Zhang, *Acta Mater.* **134**, 334 (2017).
- ⁴² C. Niu, C.R. LaRosa, J. Miao, M.J. Mills, and M. Ghazisaeidi, *Nat. Commun.* **9**, 1363 (2018).
- ⁴³ T.M. Smith, M.S. Hooshmand, B.D. Esser, F. Otto, D.W. McComb, E.P. George, M. Ghazisaeidi, and M.J. Mills, *Acta Mater.* **110**, 352 (2016).
- ⁴⁴ M. Shih, J. Miao, M. Mills, and M. Ghazisaeidi, *Nat. Commun.* **12**, 3590 (2021).
- ⁴⁵ Q.-J. Li, H. Sheng, and E. Ma, *Nat. Commun.* **10**, 3563 (2019).
- ⁴⁶ S. Zhao, Y. Osetsky, G.M. Stocks, and Y. Zhang, *Npj Comput. Mater.* **5**, 13 (2019).
- ⁴⁷ E. Ma, *Scr. Mater.* **181**, 127 (2020).
- ⁴⁸ R. Jagatramka, C. Wang, and M. Daly, *Comput. Mater. Sci.* **214**, 111763 (2022).
- ⁴⁹ S. Nag and W.A. Curtin, *Acta Mater.* **200**, 659 (2020).
- ⁵⁰ P. Chowdhury, H. Sehitoglu, W. Abuzaid, and H.J. Maier, *Int. J. Plast.* **71**, 32 (2015).
- ⁵¹ M. Daly, S. Haldar, V.K. Rajendran, J. McCrea, G.D. Hibbard, and C.V. Singh, *Mater. Sci. Eng. A* **771**, 138581 (2020).
- ⁵² S. Plimpton, *J. Comput. Phys.* **117**, 1 (1995).
- ⁵³ A. Stukowski, *Model. Simul. Mater. Sci. Eng.* **18**, 015012 (2010).
- ⁵⁴ L.K. Béland, C. Lu, Y.N. Osetskiy, G.D. Samolyuk, A. Caro, L. Wang, and R.E. Stoller, *J. Appl. Phys.* **119**, 085901 (2016).
- ⁵⁵ E. Asadi, M.A. Zaeem, A. Moitra, and M.A. Tschopp, *J. Phys. Condens. Matter* **26**, 115404 (2014).
- ⁵⁶ Y. Su, S. Xu, and I.J. Beyerlein, *J. Appl. Phys.* **126**, 105112 (2019).
- ⁵⁷ R. Ramachandramoorthy, W. Gao, R. Bernal, and H. Espinosa, *Nano Lett.* **16**, 255 (2016).
- ⁵⁸ T. Zhu, J. Li, A. Samanta, A. Leach, and K. Gall, *Phys. Rev. Lett.* **100**, 1 (2008).
- ⁵⁹ A.B. Bortz, M.H. Kalos, and J.L. Lebowitz, *J. Comput. Phys.* **17**, 10 (1975).

- ⁶⁰ H.S. Park, K. Gall, and J.A. Zimmerman, *J. Mech. Phys. Solids* **54**, 1862 (2006).
- ⁶¹ S.H. Oh, M. Legros, D. Kiener, and G. Dehm, *Nat. Mater.* **8**, 95 (2009).
- ⁶² H. Zheng, A. Cao, C.R. Weinberger, J.Y. Huang, K. Du, J. Wang, Y. Ma, Y. Xia, and S.X. Mao, *Nat. Commun.* **1**, 144 (2010).
- ⁶³ J. Shin, L.Y. Chen, U.T. Sanli, G. Richter, S. Labat, M.-I. Richard, T. Cornelius, O. Thomas, and D.S. Gianola, *Acta Mater.* **166**, 572 (2019).
- ⁶⁴ L.Y. Chen, M. He, J. Shin, G. Richter, and D.S. Gianola, *Nat. Mater.* **14**, 707 (2015).
- ⁶⁵ I. Gutierrez-Urrutia, S. Zaeferrer, and D. Raabe, *Mater. Sci. Eng. A* **527**, 3552 (2010).
- ⁶⁶ S.H. Oh, M. Legros, D. Kiener, P. Gruber, and G. Dehm, *Acta Mater.* **55**, 5558 (2007).
- ⁶⁷ Y.T. Zhu, X.Z. Liao, and X.L. Wu, *Prog. Mater. Sci.* **57**, 1 (2012).
- ⁶⁸ S. Lee, J. Im, Y. Yoo, E. Bitzek, D. Kiener, G. Richter, B. Kim, and S.H. Oh, *Nat. Commun.* **5**, 3033 (2014).
- ⁶⁹ J. Wang, Z. Zeng, C.R. Weinberger, Z. Zhang, T. Zhu, and S.X. Mao, *Nat. Mater.* **14**, 594 (2015).
- ⁷⁰ I.J. Beyerlein and C.N. Tomé, *Int. J. Plast.* **24**, 867 (2008).
- ⁷¹ C.R. Weinberger, A.T. Jennings, K. Kang, and J.R. Greer, *J. Mech. Phys. Solids* **60**, 84 (2012).
- ⁷² A.T. Jennings, C.R. Weinberger, S.-W. Lee, Z.H. Aitken, L. Meza, and J.R. Greer, *Acta Mater.* **61**, 2244 (2013).
- ⁷³ W. Cai, V. V. Bulatov, S. Yip, and A.S. Argon, *Mater. Sci. Eng. A* **309–310**, 270 (2001).
- ⁷⁴ P.M. Anderson, J.P. Hirth, and J. Lothe, *Theory of Dislocations* (Cambridge University Press, 2017).
- ⁷⁵ B. Joós and M.S. Duesbery, *Phys. Rev. Lett.* **78**, 266 (1997).
- ⁷⁶ W. Li and C. Wang, *Chinese Phys. B* **29**, 026102 (2020).

- ⁷⁷ R.O. Scattergood and D.J. Bacon, *Philos. Mag.* **31**, 179 (1975).
- ⁷⁸ D.J. Bacon, D.M. Barnett, and R.O. Scattergood, *Prog. Mater. Sci.* **23**, 51 (1980).
- ⁷⁹ A. Stukowski, *Model. Simul. Mater. Sci. Eng.* **20**, 045021 (2012).
- ⁸⁰ P. Nash, *ASM Int.* (1991).
- ⁸¹ Y. Fan, Y.N. Osetsky, S. Yip, and B. Yildiz, *Phys. Rev. Lett.* **109**, 1 (2012).
- ⁸² Y. Fan, Y.N. Osetskiy, S. Yip, and B. Yildiz, *Proc. Natl. Acad. Sci. U. S. A.* **110**, 17756 (2013).
- ⁸³ Z. Bai and Y. Fan, *Phys. Rev. Lett.* **120**, 125504 (2018).
- ⁸⁴ B. Wu, Z. Bai, A. Misra, and Y. Fan, *Phys. Rev. Mater.* **4**, 020601 (2020).

System

Sample

A^*

Planar Fault

$z, \langle 111 \rangle$

$y, \langle 11\bar{2} \rangle$

$x, \langle 1\bar{1}0 \rangle$

A

